Oxide layer containing apatite formed on Ti-25Nb-25Ta alloy treated by Two-Step Plasma Electrolytic Oxidation

Bruno Leandro Pereira[1,2], Gregory Beilner[1], Carlos Maurício Lepienski[1,3], Erico Saito Szameitat [1], Neide Kazue Kuromoto[1,4], Leonardo Luis dos Santos[1], Bor Shin Chee[2], Ana Paula Rosifini Alves Claro[5], Irineu Mazzaro[4], and Michael J D Nugent [2].

[1] Federal University of Paraná, Postgraduate Program in Materials Engineering and Science - PIPE, Curitiba, PR, Brazil

[2] Materials Research Institute MRI, Athlone Institute of Technology, Athlone, Ireland

[3] Federal University of Technology - Paraná, Department of Mechanical Engineering, Curitiba, PR, Brazil

[4] Federal University of Paraná, Physics Department, Curitiba, PR, Brazil

[5] Paulista State University, Department of Materials and Technology, Guaratinguetá-SP, Brazil

Corresponding author: Bruno L. Pereira.

Email:brnlp7@gmail.com.

Address: Dublin Rd, Bunnavally, Research Hub, East Campus, Athlone Institute of Technology, Athlone, Co. Westmeath, Ireland, N37 F6D7.

Abstract

Hydroxyapatite (HA) is a bioactive calcium phosphate capable of enhancing the implant/bone connection improving osteoconductivity and osseointegration process. However, the HA presents mechanical properties limiting its application. A good way to resolve this limitation is to combine the excellent biological properties of HA with materials with suitable mechanical behavior, like Ti-25Nb-25Ta alloy. The Ti-25Nb-25Ta alloy is composted by non-toxic and corrosion-resistant elements, presenting good biological compatibility. In this work, Plasma Electrolytic Oxidation (PEO) (using direct current-DC) was applied in conventional mode and Two-Step PEO aiming to produce a porous coating containing HA. It was not possible to produce a satisfactory coating applying conventional PEO due to successive spalling during the oxidation process. Adding a pretreatment to the conventional PEO changed the process to Two-Step PEO allowing to form a porous coating containing HA. The pretreatment was made by PEO using phosphoric electrolyte to produce a pre-coating. After that, the pre-coating was re-oxidized with calcium/phosphorus electrolyte. The Two-Step oxidized surface presented well-known good characteristics to applications in osseous implant devices such as porous formation, roughness in the micrometrical range, surface containing calcium and phosphorus, bioactive crystalline titanium oxide, and well-adhered HA formation. However, the coating morphology and chemical composition of pre-coating and Two-step oxidized surfaces were not uniform. The non-uniformity of the Two-Step oxidized surface follows a similar non-uniformity pattern of the pre-coating surface. Two distinct morphologies were identified on the Two-Step oxidized surface: a “velvety morphology” with HA formation and a highly porous morphology. Regarding the Ti-25Nb-25Ta alloy, the Two-Step oxidation produced an adhered coating with porous apatite distribution interspersed with calcium-rich porous oxide.

Keywords: β-Titanium alloys, Ti-25Nb-25Ta, Hydroxyapatite, Two-Step PEO.

1. Introduction

Hydroxyapatite (HA) is a bioactive material used to replace hard tissue being capable of improving the bonding between implants and osseous tissues. HA coatings enhance osteoconductivity, accelerate and facilitate the osseointegration process by forming a bone-like apatite that integrates strongly with the implant surface [1–3]. In addition, HA formation is considered the main prerequisite for bone-bonding ability [4]. However, the HA presents mechanical properties limiting its application. Covering apatite methods over materials, such as metallic alloys, can combine the good mechanical properties of the alloys with the biological properties of HA.

Treatments such as biomimetic method [5], Sol-gel process [6], Plasma spraying [7], Electrophoretic [8], and Electrochemical deposition [9] are capable to cover other material with apatite. However, some of these techniques may present disadvantages singly or in combination, such as poor adhesion, the necessity of great sintering temperatures, coating with cracks, long processing time, complexity in preparation, and high cost [10]. Plasma electrolytic oxidation (PEO), also is able to produce an oxide coating containing crystalline apatite on biocompatible metallic substrates like niobium (Nb) [11], tantalum (Ta) [12], and commercially pure titanium (CP-Ti) grade 4+ alloys [13]. PEO is an easy and fast process, being able to cover complex metallic geometries and possible to create suitable characteristics for osteointegration processes like porosity, well-adhered coating, corrosion-resistant interface, hydrophilic surface, favorable chemical composition, and bioactivity [14-25].

Nb, Ta, and titanium (Ti) present excellent characteristics to be used as implants in hard and soft tissues, and bioactivity after submitted to specifics superficial treatments[26–34]. Specifically, Nb, Ta, and Ti have relatively high elastic modulus (108 GPa, 186 GPa, and 118 GPa respectively) when compared to the bone values [28,31,35]. These elastic moduli

differences cause the Stress-Shielding effect in the osseous tissue. According to Wolf's Law, insufficient mechanical stimulus on osseous tissue may result in the phenomenon called bone reabsorption surround the implant and consequently decreasing the bone-implant mechanical stability [36,37]. When Ti, Ta, and Nb are alloyed, the result may create a metallic substrate with low elastic modulus like β - Titanium alloys. A β - Titanium alloy Ti-25Nb-25Ta present low modulus (55 GPa), super elastic behavior, excellent corrosion resistance [38], and superior cellular performance than titanium commercially pure [39]. Thus, the proposed study aims to treat the Ti-25Nb-25Ta alloy using Two-Step Plasma Electrolytic Oxidation to create a coating containing HA, with suitable characteristics for osteointegrables implants.

2. Experimental details

2.1. Metallurgical process

The alloy was prepared by melting pure Ti (grade 2), Nb (99.7% purity), and Ta (99.8% purity) in a controlled atmosphere (Argon gas) and following the percentage in weight 50 % of Ti, 25% of Nb, and 25% of Ta. After the alloy ingots production, the ingots were subject to two heat treatments for solubilization:

1- 950 °C for 24 h- cooling with a low gradient of decreasing temperature.

2- 850 °C for 1 h cooling with a high gradient of decreasing temperature [40].

The cylindrical ingots had 10 mm of diameter and were cut by electro-erosion wire technique with 2 mm of thickness.

To clean the surface before the electrolytic treatment, the *specimen*s were subject to a sanding process and posteriorly, the *specimen*s were ultrasonic cleaned following the procedure in the reference [11].

2.2 Plasma electrolytic oxidation (PEO) conditions

A Chroma 62024P-80-60 DC was used to supply the electrical parameters with a computer coupled to record the electrical current during PEO. The oxidations were carried out

at room temperature, with constant stirring, and using a titanium bar as a cathode. The surface alloys were exposed to the electrolyte by a hole in the wall of the electrolytic cell, fixed using a stainless steel screw, and sealed with a Viton O-ring. To perform the oxidations was used an electrolytic cell of acrylic to contain the electrolyte. The PEO processes were performed in potentiostatic mode. In this case, the voltage provided by the power source remains constant at all the oxidation time. It was used to this work two different electrolytes:

1. Phosphoric solution:1 mol.L^{-1} H_3PO_4 (80 % vol.) + 35 % hydrogen peroxide (20% vol.).
2. Calcium + Phosphorus electrolyte: 0.5 mol.L^{-1} $Ca(CH_3CO_2)_2 \cdot H_2O$ (80% vol.) + Phosphoric solution (20% vol.)

To verify the influence of the pre-layer, the oxidations were performed in conventional PEO mode (without pre-layer) and Two-Step PEO. The conventional PEO was conducted using the same experimental parameters as the second step of Two-Step PEO.

2.2.1 Conventional PEO conditions

The electrolyte used to this condition was the Calcium + Phosphorus electrolyte and a voltage of 380V was applied during 60s.

2.2.2 Two-Step PEO conditions

This process was made in two steps and each step had different voltage and electrolyte. The condition used was based in our previous work using niobium[11]. However, the same condition used to Nb did not produce a satisfactory coating and it was necessary to regulate the experimental parameters. The better condition found was presented in this work:

2.2.2.1 First-Step Plasma electrolytic oxidation (PEO) conditions

In the first step, the power supply provided 300 V, during 30s, using a Phosphoric solution. Subsequently, the *specimen*, counter-electrode, stirrer magnetic bar, and the electrolytic cell were cleaned with distilled water.

2.2.2.2 Second-Step PEO conditions

For the next step, the electrolyte was changed to Calcium + Phosphorus electrolyte and a voltage of 380V was applied during 60s. This condition has the same parameters of the conventional PEO.

2.3 Surface characterization

By using Scanning Electronic Microscopy SEM (TESCAN Vega 3 LMU) and Energy Dispersive X-ray EDS technique, the surface morphology, and chemical composition were analyzed. The EDS was running in three different modes:

(i) In mapping mode for visualizing the elemental concentration distributed over the oxidized areas;

(ii) line mode over the grooves formed by the nanoscratch tests to identify where the oxide was completely removed;

(iii) Pointing mode to quantify the atomic percentage in distinct morphologies.

Crystalline phases were characterized by X-ray diffraction (XRD) in the $20° \leq 2\theta \leq 75°$ range, with Cu Kα radiation (λ=1.54 Å), using a monochromatic filter, and Bragg-Brentano pattern.

As the reference for hydroxyapatite, we used a bioactive treated Titanium *specimen*, which presented an HA layer after soaked, during 30 d, in simulated body fluid SBF (to make SBF see [41]). This reference *specimen* was treated using a process in a previous result [42].

2.4 Scratch test

The scratch test was made by a ZHN Nanoindenter (Zwick-Roell), employing an increasing force in the 0 – 300 mN range. A spherical diamond tip (radius 5µm) produced three scratches of 300 µm onto the Two-Step oxidized surface.

2.5 Thickness Measurement

Setting as thickness zero the point where the region that started to expose the metallic substrate on the groove made by scratch test, we apply the stereomicroscopy. The stereomicroscopy was done using SEM TESCAN. Through images superposition, a 3D perspective was created with a colorized heights-based system.

3. Results and discussion

3.1 Conventional Plasma electrolytic oxidation (PEO)

This test was performed using only the second step of the Two-Step PEO process. That is, it was performed in a single step, applying a constant voltage of 380 V for 60 s, using calcium and phosphorus electrolyte. This oxidation was performed to observe the differences between conventional mode and Two-Step process.

Fig. 1 shows the current density versus time curve of the single-step process. In this curve, it is possible to observe a more intense peak at the beginning and several other smaller peaks. At the beginning of the oxidation process, the natural oxide layer is very thin. This layer is an electrical insulator. Therefore, at this stage, the current density is high and then decreases rapidly due to the growth of oxide layer thickness during the oxidation process. During PEO it is normal that small oscillations in noise format occur in the current density curve. This noise in the curve is due to the dielectric breakdowns being possible to observe in this stage the spark formations[15]. However, the well-defined peaks, positioned after the first intense peak, are characteristic of successive spalling and formation of the oxide that occurred during the conventional PEO process.

Fig. 2 shows the SEM images of oxidized surfaces produced by conventional PEO. Through the images, it is possible to observe grooves forming parallel lines. That is, after the successive formation and spalling the formed coating remnant was quite thin because it did not was able to cover the grooves produced by the sanding process present on the original bulk.

As previously mentioned, this surface did not keep the oxide adhered to the surface during the PEO process, presenting successive oxide formations and spalling during the oxidation. As a consequence of the spalling and formation cycles, it is possible to observe the presence of remnant fragments on the surface as highlighted in the 10kx magnification image (Fig. 2).

EDS analysis revealed that the surface with the sanding grooves (point 2) has Ca / P ratio ~ 0.6 and the remnant fragments (points 1 and 3) Ca / P ~ 2. That is, there was no formation of HA on the surface treated by conventional PEO.

A wide range of conventional PEO experimental parameters was applied to Ti-25Nb-25Ta alloy have been previously performed, however, like this one, they did not form adhered coatings or formed adherent coatings, but without HA. So, it was decided to add a pretreatment and run PEO in two steps as shown in the next subsection.

3.2 Two-Step Plasma electrolytic oxidation (PEO)

Fig. 3 shows the curves of Two-Step Oxidation of the Ti-25Nb-25Ta alloy. The gray and black lines describe the electric current behavior at the first step and the second step, respectively. Differently from the conventional PEO curve, the Two-Step PEO curve did not exhibit spalling characteristics during the oxidation process. As expected, the first oxidation

has a taller peak in the curve due to the surface *specimen*, at this moment, which has poor electrical resistance. Over time, reactions occurring in the metal surface produces a dielectric coating that increases with the passing of the electrical current. The thickness growth provokes the electrical current decrease. When the phosphoric electrolyte was changed to calcium + phosphorus electrolyte and the voltage was raised from 300V to 380 V, another current peak appears, and over time, the current again drops down after the electrochemical process increases the electrical resistance. These curves in an independent way are characteristic of the PEO process using constant voltage [43,44].

Fig. 4 shows the *specimen* two-step oxidized surface. It was possible to distinguish two different morphologies: a morphology containing fewer pores number with larger pore size and morphology that seems covered by the previously mentioned. The upper morphology has a “velvety texture”, which appears a morphology obtained by Two-Step PEO in Niobium using a resembling treatment [11]. In addition, this morphology presents a few similarities with tooth cementum [45]. The main difference between the coatings on Nb and Ti-25Nb-25Ta was the possibility to produce a more regular surface on Niobium using similar treatment.

The measured roughness remains on the microscale surface roughness. As cited, when occurs the contact between implant and blood there is a dynamic cellular activity preliminary with leukocytes, platelets, and the action of structural proteins [46]. The initial protein anchorage depends on surface topography (for example, microtextured-morphology on Titanium presented better anchorage of these initial proteins than Titanium turned)[46]. In addition, Lossdörfer *et al.* found a favorable relation between micro-rough topographies and decreasing of osteoclast (cells responsible to reabsorb osseous tissue) formation with a consequent intensification of osteogenesis [47].

By observing Fig. 5 and Fig. 6, it is possible to see the non-uniformity on the pre-treatment and on the final treatment. There are different morphologies with dissimilar chemical

compositions: “island containing pores” with higher phosphorus atomic percentage (point 1-Fig. 5) and regions around of the islands containing grooves with a higher metal percentage (point 2-Fig. 5). However, the atomic percentage of oxygen does not change significantly in the two different regions.

When the *specimen* was re-oxidized, the surface morphology completely changes. The pore size increases and the shape changed to volcano form. Moreover, the chemical and morphological non-uniformity is present, also, after the Two-Step treatment. Chemically, in the point 1-Fig 5, there are higher phosphorus and lower metal atomic percentage. The Ca/P ratio is also higher (Ca/P = 2.98) than the velvety region (point 2- Ca/P = 1.56). The Ca/P ratio in the velvety region is close to the expected to the hydroxyapatite (Ca/P = 1.6), which is an indicator of the coating containing HA was produced in some regions over the oxidized surface.

In an interesting way, as well as, the second treatment produced a non-uniform surface as the pre-treatment. We can infer the morphology was affected by two levels of PEO treatment. It was observed by our previous work, using the same alloy and phosphoric electrolyte, the PEO produced two clearly distinct porous formations with different phosphorus atomic percentage. The Ti-25Nb-25Ta shown a microstructure with dimension grains in the range of the two different formation areas (see reference [40] and [48]). Fushimi and coworkers demonstrated a heterogeneous thickness formation of titanium oxide in different crystal grains of titanium substrate treated by anodization process [49]. Another author verified the influence of the Ti substrate orientation in the process of oxide formation and supposed that the ionic transfer between metal and oxide is controlled by the substrate packing density [50]. To this alloy, there are clearly morphologically and chemically distinct regions with similar dimensions to the grain boundaries of the Ti-25Nb-25Ta alloy. It is possible to assume the substrate orientation of Ti-25Nb-25Ta influenced the apatite

formation. The two-step oxidation of the alloy produced a surface with good porous apatite distribution, however, the formation is non-continuous and interspersed with porous oxide.

Fig.7 shows the XRD pattern of the sanded substrate, titanium oxidized soaked in simulated body fluid SBF during 30 days (Ti+HA), and the Two-Step oxidized surface (*specimen*). Recalling that the oxidized titanium *specimen* covered with HA was used only for comparison with HA peaks found for the *specimen* produced in this work. Comparing the Two-Step oxidized with the substrate patterns is clearly that four peaks are coincident. Three peaks (38.7°, 55.7°, and 70.04°) are referent to the alloy cubic system. A similar pattern was found by Bertran *et al.*[38] and Cimpean *et al.* [39]. However, our diffractogram presents an additional angle of 42.7° to the substrate. It is not clear what the crystallographic pattern is correspondent to this mentioned angle since there is only one peak. This peak corresponds to a titanium metastable phase α”(martensite)[40]. Excluding the Ti and TiO_2 crystalline (anatase and rutile) peaks of the *specimen* covered by HA, only the HA peaks remain. Comparing these peaks with the Two-Step oxidized *specimen* peaks, it was possible to see common angles at 23.0°, 25.8°, 31.7°, 46.7°, 48.1°, and 49.4°. These angles correspond to hydroxyapatite [11], being the peak nearby to the 31.7° usually intense and large (see [51] page 4634, [42] page 21, and [30] page 931), because this peak is composed by 3 close peaks. In addition, relating the XRD HA patterns with a previous work [11], which reached a coating containing HA through the Two-Step oxidation on niobium, there is a similarity. Despite the apatite non-uniform formation, the coating produced using Ti-25Nb-25Ta presents more defined HA peaks than the obtained on Niobium previously (see reference [11]).

Fig. 8 shows the scratch test made over a region with a Ca/P ratio ~1.6. Through the scratch test was possible to obtain a qualitative measurement of the coating adhesion. The scratch length was 300 μm applying a crescent load of 0 to 300 mN. It was made three scratches, as can be seen in Fig. 9, and was chosen to show the groove that exposed the metallic substrate (other two scratches did not be capable to remove completely the coating).

The method used was EDS in line mode along the groove. The EDS provided the atomic percentage of the elements that compound the coating. However, to demonstrate the load able to expose the substrate a unique metallic element is enough – in this case, was chosen Titanium atomic percentage. By observing Fig. 8, there is an abrupt increase of Titanium atomic percentage to the correspondent load of 275 mN and accompanied by a lighter region in the MEV image to the respective load. In other words, three scratches were made and one presented a critical load of 275 mN, which was capable to remove the oxide coating.

In this work, we proposed a different way to measure the coating thickness. Analyzing Fig. 8 is possible to have a starting point where the coating was completely removed by the scratch test. Then, it was marked as a reference point – height zero. After that, using stereomicroscopy was possible to create an image with a 3D perspective applying a scaled system based on colors, as can be seen in Fig. 9. Although this technique does not allow us to see the three (or two) layers that normally form the coating made by PEO, this perspective presents advantages when compared with cross-sectional images due to roughness and variations on the thickness, which can be better analyzed using a 3D perspective. Scratch, EDS, and stereomicroscopy to obtain the thickness are easy and fast techniques, and they are not limited to a single line and are able more efficiently to give points of maximum, minimum, and anomalous heights.

The coating thickness is mainly in the 6 – 16 μm range. However there some anomalous points that can reach less than 4 μm and more than 18 μm. The highest regions are placed on the groove borders close to the end, due to oxide accumulation caused by scratching.

4. Conclusions

In this work, Ti-25Nb-25Ta alloy was successfully oxidized by Two-Step PEO. The process consisted of oxidizing the alloy using a phosphate-based electrolyte to create a pre-

coating, and after, the first coating was re-oxidized using an electrolyte containing calcium and phosphate ions.

The phosphorus pre-coating played an important role in the formation of the well-adhered apatite coating and prevented that during the oxidation process there was successive spalling of the oxide coating on the alloy.

The treatment produced a coating with micrometric roughness, thickness in the 6 – 16 μm range, and there were:

1. A formation of two distinct porous morphologies with two different Ca/P ratio. The velvety morphology presented the Ca/P ratio (1.57) close to the hydroxyapatite (1.67) value and the highest porous morphology showed a higher Ca/P ratio (2.98).
2. The non-uniformity of the Two-Step oxidized surface follows the non-uniformity of the pre-coating surface.
3. Crystalline hydroxyapatite formation in the coating was confirmed by the XRD technique. In addition, bioactive TiO_2 phases were present in the coating.
4. The coating produced show good adherence and non-uniform behavior. Scratching 3 times using a nanoindenter with a maximum load of 300 mN, only one scratch was capable to remove completely the coating containing HA to a critical load of 275 mN.
5. For Ti-25Nb-25Ta alloy, the two-step oxidation produced a surface with good porous apatite distribution interspersed with calcium-rich porous oxide.

5. Acknowledgments

The authors would like to thank the CAPES, GOI (Government of Ireland), Electron Microscopy Center, and LORXI (FINEP CT-INFRA 793/2004 & 3080/2011) at UFPR.

References

[1] K. Søballe, E.S. Hansen, H. Brockstedt-Rasmussen, C. Bünger, Hydroxyapatite Coating Converts Fibrous Tissue to bone Around Loaded Implants, J Bone Jt. Surg. 75 (1993) 270–278. https://doi.org/10.1302/0301-620X.75B2.8444949.

[2] M. Geetha, a. K. Singh, R. Asokamani, a. K. Gogia, Ti based biomaterials, the ultimate choice for orthopaedic implants – A review, Prog. Mater. Sci. 54 (2009) 397–425. https://doi.org/10.1016/j.pmatsci.2008.06.004.

[3] M. Mucalo, Hydroxyapatite (HAp) for Biomedical Applications, Elsevier Science, 2015. https://books.google.com.br/books?id=CkSdBAAAQBAJ.

[4] X. Liu, P. Chu, C. Ding, Surface modification of titanium, titanium alloys, and related materials for biomedical applications, Mater. Sci. Eng. R Reports. 47 (2004) 49–121. https://doi.org/10.1016/j.mser.2004.11.001.

[5] C. Chaves Guedes Silva, E. Cristina da Silva Rigo, J. Marchi, A. Helena de Almeida Bressiani, J. Carlos Bressiani, Hydroxyapatite Coating on Silicon Nitride Surfaces Using the Biomimetic Method, Mater. Res. 11 (2008) 47–50. https://doi.org/10.1590/S1516-14392008000100009.

[6] C. Domínguez-trujillo, E. Peón, E. Chicardi, H. Pérez, J.A. Rodríguez-ortiz, J.J. Pavón, Surface & Coatings Technology Sol-gel deposition of hydroxyapatite coatings on porous titanium for biomedical applications, Surf. Coat. Technol. 333 (2018) 158–162. https://doi.org/10.1016/j.surfcoat.2017.10.079.

[7] T.J. Levingstone, M. Ardhaoui, K. Benyounis, L. Looney, J.T. Stokes, Plasma sprayed hydroxyapatite coatings: Understanding process relationships using design of experiment analysis, Surf. Coatings Technol. 283 (2015) 29–36. https://doi.org/10.1016/j.surfcoat.2015.10.044.

[8] A. Tahmasbi Rad, M. Solati-Hashjin, N.A.A. Osman, S. Faghihi, Improved bio-physical performance of hydroxyapatite coatings obtained by electrophoretic deposition at dynamic voltage, Ceram. Int. 40 (2014) 12681–12691. https://doi.org/10.1016/j.ceramint.2014.04.116.

[9] D. Qiu, A. Wang, Y. Yin, Applied Surface Science Characterization and corrosion behavior of hydroxyapatite / zirconia composite coating on NiTi fabricated by electrochemical deposition, Appl. Surf. Sci. 257 (2010) 1774–1778. https://doi.org/10.1016/j.apsusc.2010.09.014.

[10] W.S.W. Harun, R.I.M. Asri, J. Alias, F.H. Zulkifli, K. Kadirgama, S.A.C. Ghani, J.H.M. Shariffuddin, A comprehensive review of hydroxyapatite-based coatings adhesion on metallic biomaterials, Ceram. Int. 44 (2018) 1250–1268. https://doi.org/10.1016/j.ceramint.2017.10.162.

[11] B.L. Pereira, C.M. Lepienski, I. Mazzaro, N.K. Kuromoto, Apatite grown in niobium by two-step plasma electrolytic oxidation, Mater. Sci. Eng. C. 77 (2017) 1235–1241. https://doi.org/10.1016/j.msec.2016.10.073.

[12] M. Sowa, M. Woszczak, A. Kazek-Kęsik, G. Dercz, D.M. Korotin, I.S. Zhidkov, E.Z. Kurmaev, S.O. Cholakh, M. Basiaga, W. Simka, Influence of process parameters on

plasma electrolytic surface treatment of tantalum for biomedical applications, Appl. Surf. Sci. 407 (2017) 52–63. https://doi.org/10.1016/j.apsusc.2017.02.170.

[13] S. Lederer, S. Sankaran, T. Smith, W. Fürbeth, Surface & Coatings Technology Formation of bioactive hydroxyapatite-containing titania coatings on CP-Ti 4 + alloy generated by plasma electrolytic oxidation, Surf. Coat. Technol. 363 (2019) 66–74. https://doi.org/10.1016/j.surfcoat.2019.02.030.

[14] A. Lugovskoy, M. Zinigr, Plasma Electrolytic Oxidation of Valve Metals, in: Mater. Sci. - Adv. Top., InTech, 2013. https://doi.org/10.5772/54827.

[15] a. L. Yerokhin, X. Nie, a. Leyland, a. Matthews, S.J. Dowey, Plasma electrolysis for surface engineering, Surf. Coatings Technol. 122 (1999) 73–93. https://doi.org/10.1016/S0257-8972(99)00441-7.

[16] Y. Ge, Y. Wang, Y. Cui, Y. Zou, L. Guo, J. Ouyang, D. Jia, Applied Surface Science Growth of plasma electrolytic oxidation coatings on Nb and corresponding corrosion resistance, Appl. Surf. Sci. 491 (2019) 526–534. https://doi.org/10.1016/j.apsusc.2019.06.114.

[17] E. Ahounbar, S. Mohammad, M. Khoei, H. Omidvar, Characteristics of in-situ synthesized Hydroxyapatite on TiO 2 ceramic via plasma electrolytic oxidation, Ceram. Int. 45 (2019) 3118–3125. https://doi.org/10.1016/j.ceramint.2018.10.206.

[18] I.V. Lukiyanchuk, V.S. Rudnev, L.M. Tyrina, I.V. Chernykh, Plasma electrolytic oxide coatings on valve metals and their activity in CO oxidation, Appl. Surf. Sci. 315 (2014) 481–489. https://doi.org/10.1016/j.apsusc.2014.03.040.

[19] R. Vasili, L. Zekovi, Applied Surface Science Characterization of oxide coatings formed on tantalum by plasma electrolytic oxidation in 12-tungstosilicic acid, 257 (2011) 10590–10594. https://doi.org/10.1016/j.apsusc.2011.07.055.

[20] O.A. Galvis, D. Quintero, J.G. Castaño, H. Liu, G.E. Thompson, P. Skeldon, F. Echeverría, Surface & Coatings Technology Formation of grooved and porous coatings on titanium by plasma electrolytic oxidation in H 2 SO 4 / H 3 PO 4 electrolytes and effects of coating morphology on adhesive bonding, Surf. Coat. Technol. 269 (2015) 238–249. https://doi.org/10.1016/j.surfcoat.2015.02.036.

[21] S.L. Aktuğ, S. Durdu, E. Yalçın, K. Çavuşoğlu, M. Usta, Bioactivity and biocompatibility of hydroxyapatite-based bioceramic coatings on zirconium by plasma electrolytic oxidation, Mater. Sci. Eng. C. 71 (2017) 1020–1027. https://doi.org/10.1016/j.msec.2016.11.012.

[22] Z. Zhang, B. Gu, W.E.I. Zhu, L. Zhu, Integrin - mediated osteoblastic adhesion on a porous manganese - incorporated TiO 2 coating prepared by plasma electrolytic oxidation, (2013) 707–714. https://doi.org/10.3892/etm.2013.1204.

[23] H.T. Siu, H.C. Man, Fabrication of bioactive titania coating on nitinol by plasma electrolytic oxidation, Appl. Surf. Sci. 274 (2013) 181–187. https://doi.org/10.1016/j.apsusc.2013.03.008.

[24] T.-E. Park, H.-C. Choe, W. a. Brantley, Bioactivity evaluation of porous TiO2 surface formed on titanium in mixed electrolyte by spark anodization, Surf. Coatings Technol. 235 (2013) 706–713. https://doi.org/10.1016/j.surfcoat.2013.08.051.

[25] B. Leandro, A. Rossetto, C. Maurício, I. Mazzaro, N. Kazue, Niobium treated by Plasma Electrolytic Oxidation with calcium and phosphorus electrolytes, J. Mech. Behav. Biomed. Mater. 77 (2018) 347–352. https://doi.org/10.1016/j.jmbbm.2017.08.010.

[26] G. Ramírez, S.E. Rodil, H. Arzate, S. Muhl, J.J. Olaya, Niobium based coatings for dental implants, Appl. Surf. Sci. 257 (2011) 2555–2559. https://doi.org/10.1016/j.apsusc.2010.10.021.

[27] E. Asselin, T.M. Ahmed, A. Alfantazi, Corrosion of niobium in sulphuric and hydrochloric acid solutions at 75 and 95 ° C, 49 (2007) 694–710. https://doi.org/10.1016/j.corsci.2006.05.028.

[28] H. Matsuno, A. Yokoyama, F. Watari, M. Uo, T. Kawasaki, Biocompatibility and osteogenesis of refractory metal implants, titanium, hafnium, niobium, tantalum and rhenium, Biomaterials. 22 (2001) 1253–1262. https://doi.org/10.1016/S0142-9612(00)00275-1.

[29] T. Miyazaki, Development of bioactive materials based on bone-bonding mechanism on metal oxides, J. Ceram. Soc. Japan. 116 (2008) 260–264. https://doi.org/10.2109/jcersj2.116.260.

[30] T. Miyazaki, H. Kim, T. Kokubo, C. Ohtsuki, T. Nakamura, Apatite-Forming Ability of Niobium Oxide Gels in a Simulated Body Fluid, J. Ceram. Soc. Japan. 109 (2001) 929–933.

[31] B.R. Levine, S. Sporer, R.A. Poggie, C.J. Della Valle, J.J. Jacobs, Experimental and clinical performance of porous tantalum in orthopedic surgery, Biomaterials. 27 (2006) 4671–4681. https://doi.org/10.1016/j.biomaterials.2006.04.041.

[32] P. Zhang, Z. Zhang, W. Li, M. Zhu, Applied Surface Science Effect of Ti-OH groups on microstructure and bioactivity of TiO 2 coating prepared by micro-arc oxidation, Appl. Surf. Sci. 268 (2013) 381–386. https://doi.org/10.1016/j.apsusc.2012.12.105.

[33] Q. Chen, G. a. Thouas, Metallic implant biomaterials, Mater. Sci. Eng. R Reports. 87 (2015) 1–57. https://doi.org/10.1016/j.mser.2014.10.001.

[34] M. Niinomi, Recent metallic materials for biomedical applications, Metall. Mater. Trans. A. 33 (2002) 477–486. https://doi.org/10.1007/s11661-002-0109-2.

[35] J.Y. Rho, R.B. Ashman, C.H. Turner, Young's modulus of trabecular and cortical bone material: Ultrasonic and microtensile measurements, J. Biomech. 26 (1993) 111–119. https://doi.org/10.1016/0021-9290(93)90042-D.

[36] M.G. Joshi, S.G. Advani, F. Miller, M.H. Santare, Analysis of a femoral hip prosthesis designed to reduce stress shielding, J. Biomech. 33 (2000) 1655–1662. https://doi.org/10.1016/S0021-9290(00)00110-X.

[37] A. Biomaterial, Overview of Biomaterials, (2003). https://doi.org/10.1361/hmmd2003p001.

[38] E. Bertrand, T. Gloriant, D.M. Gordin, E. Vasilescu, P. Drob, C. Vasilescu, S.I. Drob, Synthesis and characterisation of a new superelastic Ti-25Ta-25Nb biomedical alloy, J. Mech. Behav. Biomed. Mater. 3 (2010) 559–564.

https://doi.org/10.1016/j.jmbbm.2010.06.007.

[39] A. Cimpean, V. Mitran, C.M. Ciofrangeanu, B. Galateanu, E. Bertrand, D. Gordin, D. Iordachescu, T. Gloriant, Osteoblast cell behavior on the new beta-type Ti – 25Ta – 25Nb alloy, Mater. Sci. Eng. C. 32 (2012) 1554–1563. https://doi.org/10.1016/j.msec.2012.04.042.

[40] M.R. Seixas, B.J. C, R.T. Konatu, P.J. A, A.C.A.P. R, Mechanical and Microstructural Characterization of the Ti-25Ta-25Nb Alloy for Dental Applications, 869 (2016) 935–939. https://doi.org/10.4028/www.scientific.net/MSF.869.935.

[41] T. Kokubo, H. Takadama, How useful is SBF in predicting in vivo bone bioactivity?, Biomaterials. 27 (2006) 2907–15. https://doi.org/10.1016/j.biomaterials.2006.01.017.

[42] B.L. Pereira, P. Tummler, C.E.B. Marino, P.C. Soares, N.K. Kuromoto, Titanium bioactivity surfaces obtained by chemical / electrochemical treatments, Rev. Matéria. 19 (2014) 16–23.

[43] N.K. Kuromoto, R.A. Simão, G.A. Soares, Titanium oxide films produced on commercially pure titanium by anodic oxidation with different voltages, 58 (2007) 114–121. https://doi.org/10.1016/j.matchar.2006.03.020.

[44] Z. Huan, L.E. Fratila-Apachitei, I. Apachitei, J. Duszczyk, Porous NiTi surfaces for biomedical applications, Appl. Surf. Sci. 258 (2012) 5244–5249. https://doi.org/10.1016/j.apsusc.2012.02.002.

[45] Z.X. Chen, Y. Takao, W.X. Wang, T. Matsubara, L.M. Ren, Surface characteristics and in vitro biocompatibility of titanium anodized in a phosphoric acid solution at different voltages., Biomed. Mater. 4 (2009) 065003. https://doi.org/10.1088/1748-6041/4/6/065003.

[46] A. Jokstad, Osseointegration and Dental Implants, Wiley, 2009. https://books.google.ie/books?id=ktF5NW4qk48C.

[47] S. Lossdörfer, Z. Schwartz, L. Wang, C. Lohmann, J. Turner, M. Wieland, D. Cochran, B. Boyan, Microrough implant surface topographies increase osteogenesis by reducing osteoclast formation and activity., J. Biomed. Mater. Res. - Part A. 70 A (2004) 361–369. https://doi.org/10.1002/jbm.a.30025.

[48] G. Beilner, TRATAMENTO SUPERFICIAL NA LIGA Ti-25Nb-25Ta PARA IMPLANTES BIOMÉDICOS, Federal University of Parana, 2018.

[49] K. Fushimi, T. Okawa, K. Azumi, M. Seo, J.E. Soc, K. Fushimi, T. Okawa, K. Azumi, M. Seo, Heterogeneous Growth of Anodic Oxide Film on a Polycrystalline Titanium Electrode Observed with a Scanning Electrochemical Microscope Heterogeneous Growth of Anodic Oxide Film on a Polycrystalline Titanium Electrode Observed with a Scanning Electrochemical Microscope, 147 (2000) 524–529. https://doi.org/10.1149/1.1393227.

[50] S. Kudelka, A. Michaelis, J.W. Schultze, Electrochemical Characterisation of Oxide Layers on Single Grains of a Polycrystalline Ti-Sample, (1995) 1020–1027.

[51] X.-X. Wang, W. Yan, S. Hayakawa, K. Tsuru, A. Osaka, Apatite deposition on thermally and anodically oxidized titanium surfaces in a simulated body fluid,

Biomaterials. 24 (2003) 4631–4637. https://doi.org/10.1016/S0142-9612(03)00357-0.

List of Fig. captions.

Figure 1. Current density vs. time curve obtained by collecting data during the conventional PEO process.

Figure 2. SEM image showing surface morphologies of the specimen treated by conventional PEO.

Figure 3: Current density vs. time curve obtained by collecting data during the Two-Step PEO process. The gray curve represents the first step oxidation and the black curve represents the second step process.

Figure 4: SEM image showing surface morphologies of the *specimen* treated by Two-Step PEO with the respective Ra and Sa roughness.

Figure 5: SEM image showing the morphologies of the pre-treated surface with the respective chemical composition in punctual and mapping mode.

Figure 6: SEM image showing the morphologies of the Two-Step oxidized surface with the respective chemical composition in punctual and mapping mode.

Figure 7: XRD diffractions pattern comparing the PEO treated *specimen* (black curve) with the sanded Ti-25Nb-25Ta alloy and titanium treated covered with hydroxyapatite (gray curves).

Figure 8: The Titanium atomic percentage (measured by EDS in line mode along of the groove) as a function of load applied by the scratch test.

Figure 9: 3D image perspective of the nanoscratches obtained by stereomicroscopy.

List of Figures.

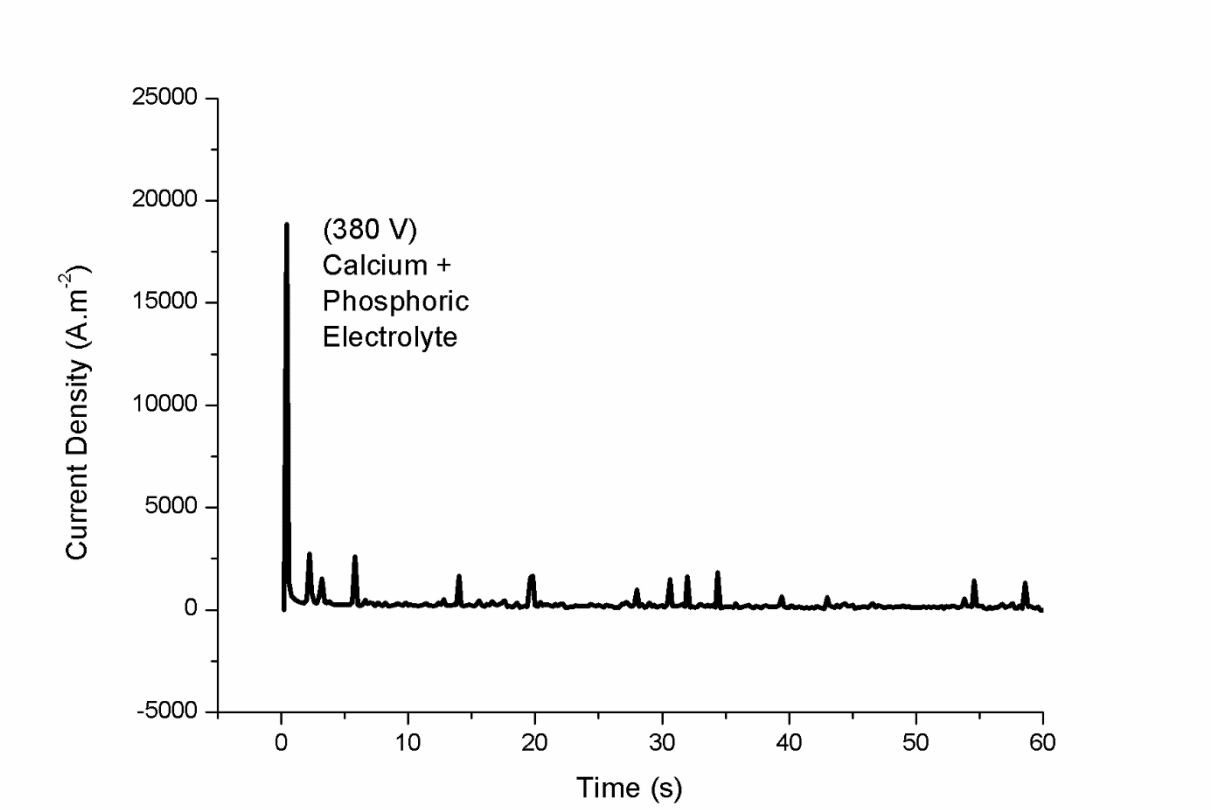

Figure 1.

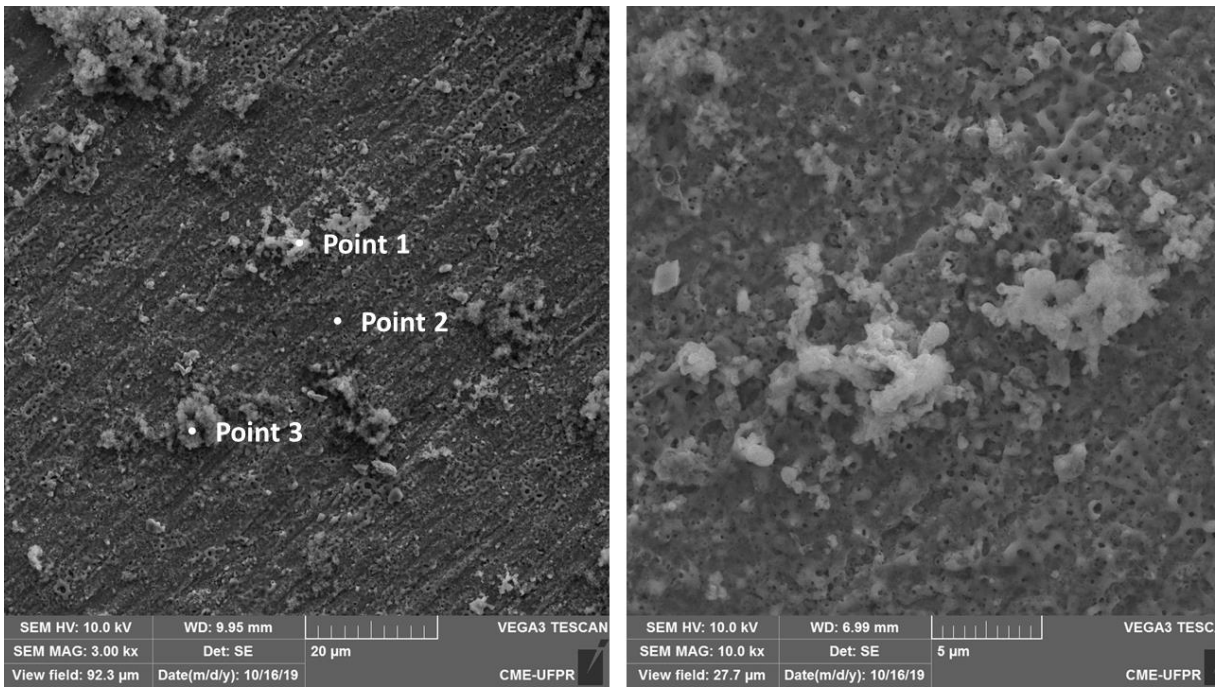

Figure 2

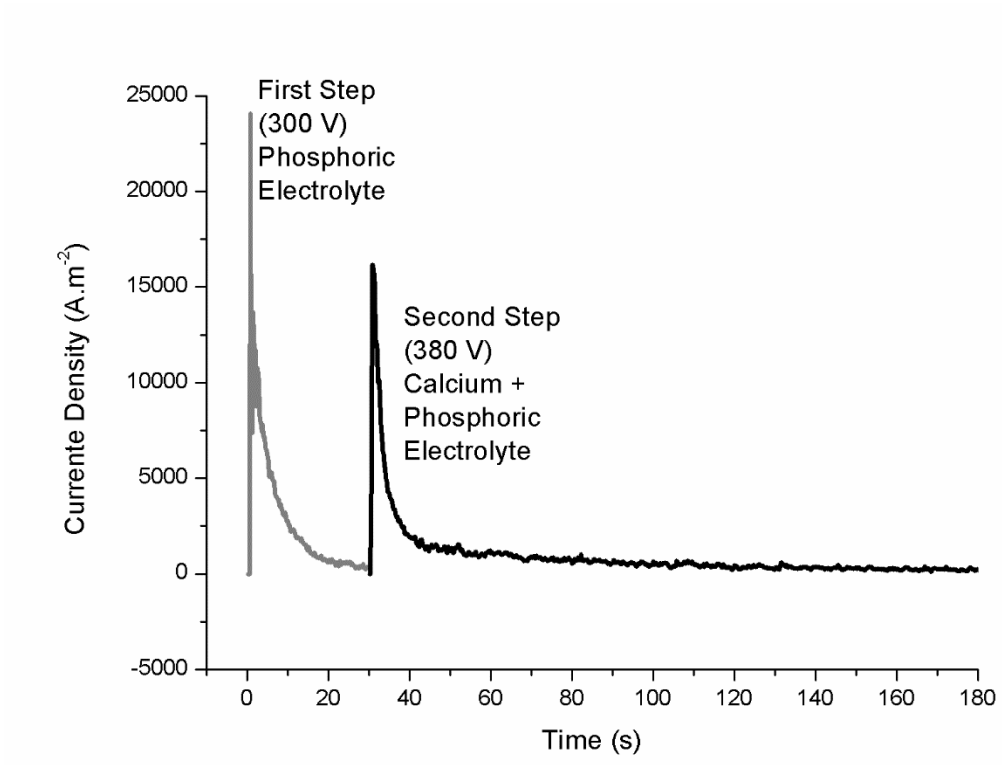

Figure 3.

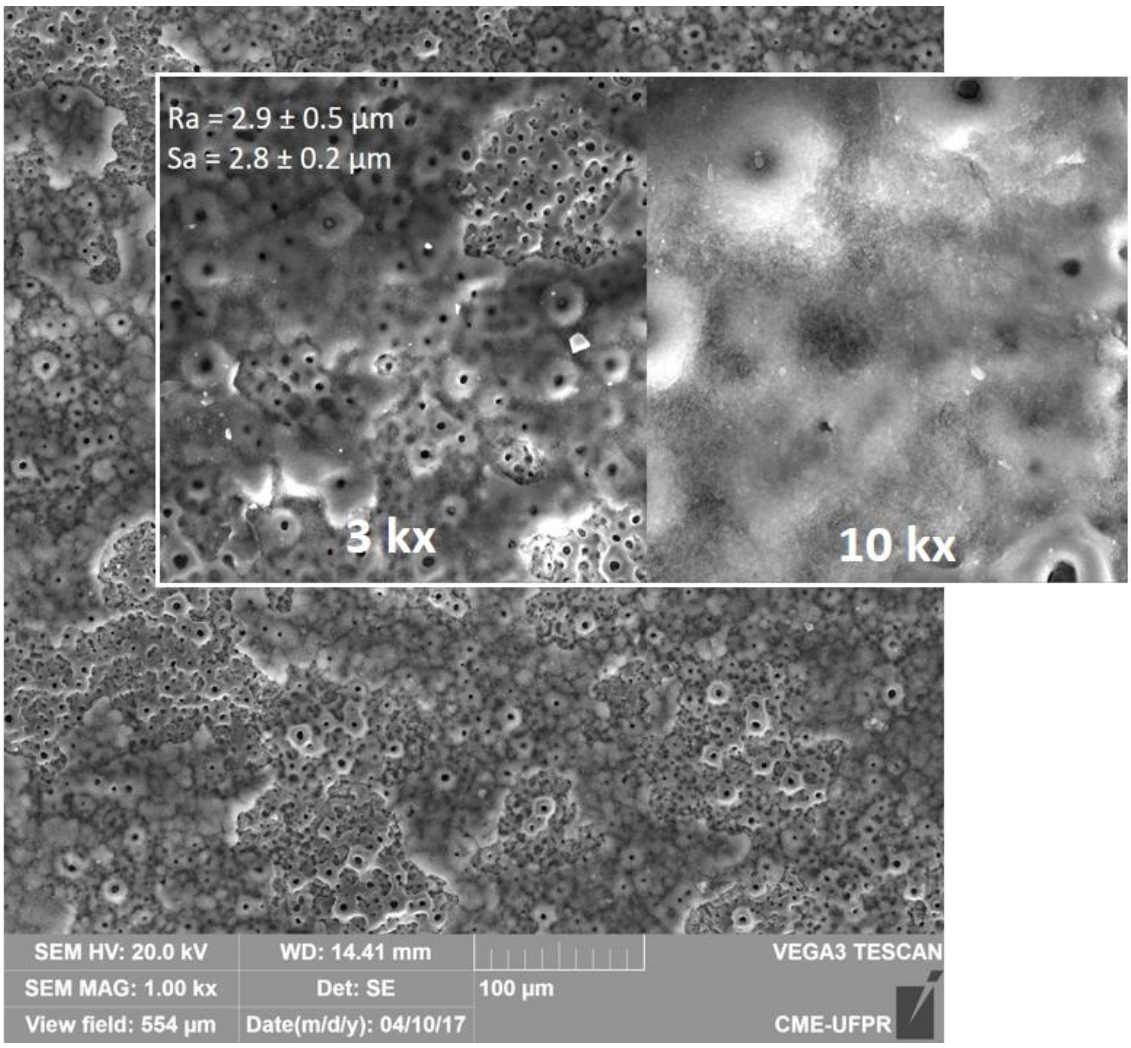
Ra = 2.9 ± 0.5 µm
Sa = 2.8 ± 0.2 µm
3 kx
10 kx
SEM HV: 20.0 kV
WD: 14.41 mm
VEGA3 TESCAN
SEM MAG: 1.00 kx
Det: SE
100 µm
View field: 554 µm
Date(m/d/y): 04/10/17
CME-UFPR

Figure 4.

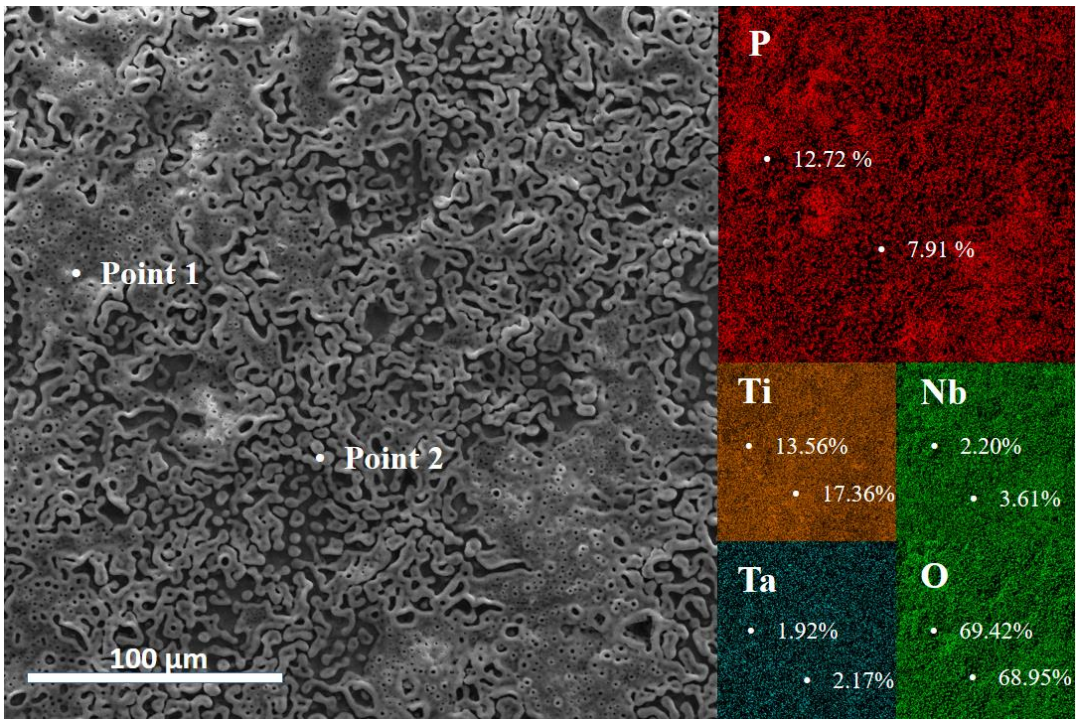

Figure 5.

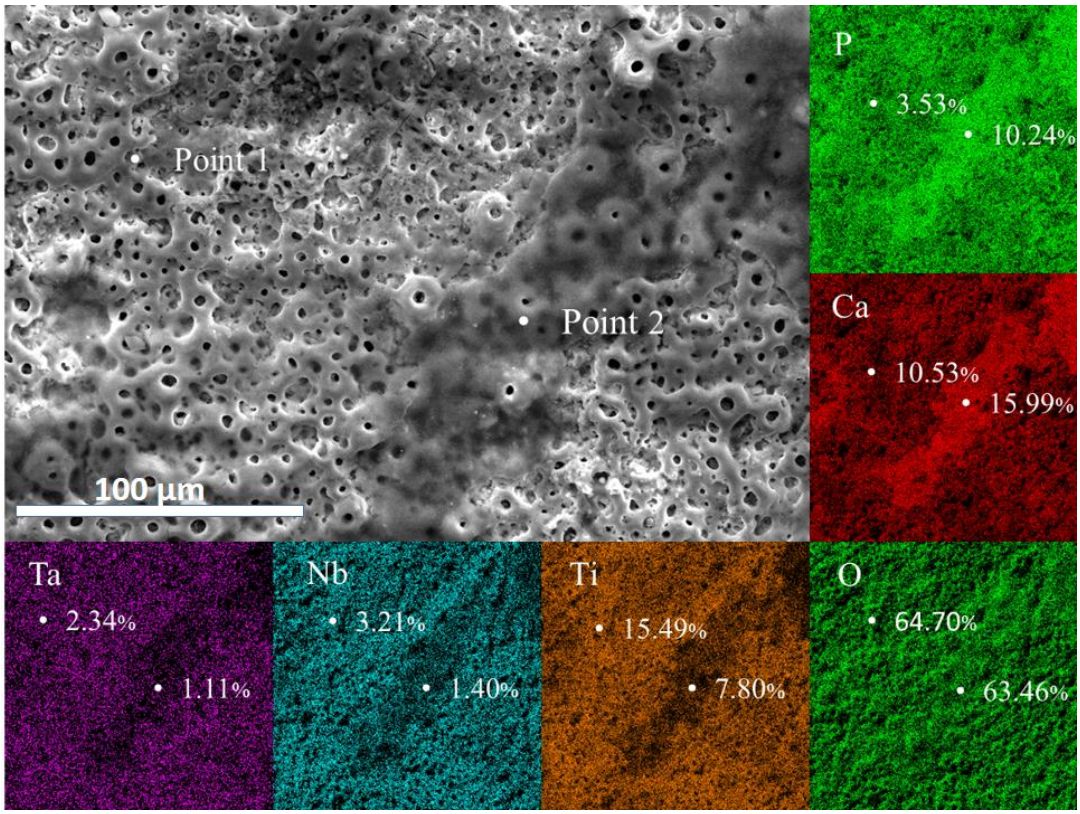

Figure 6.

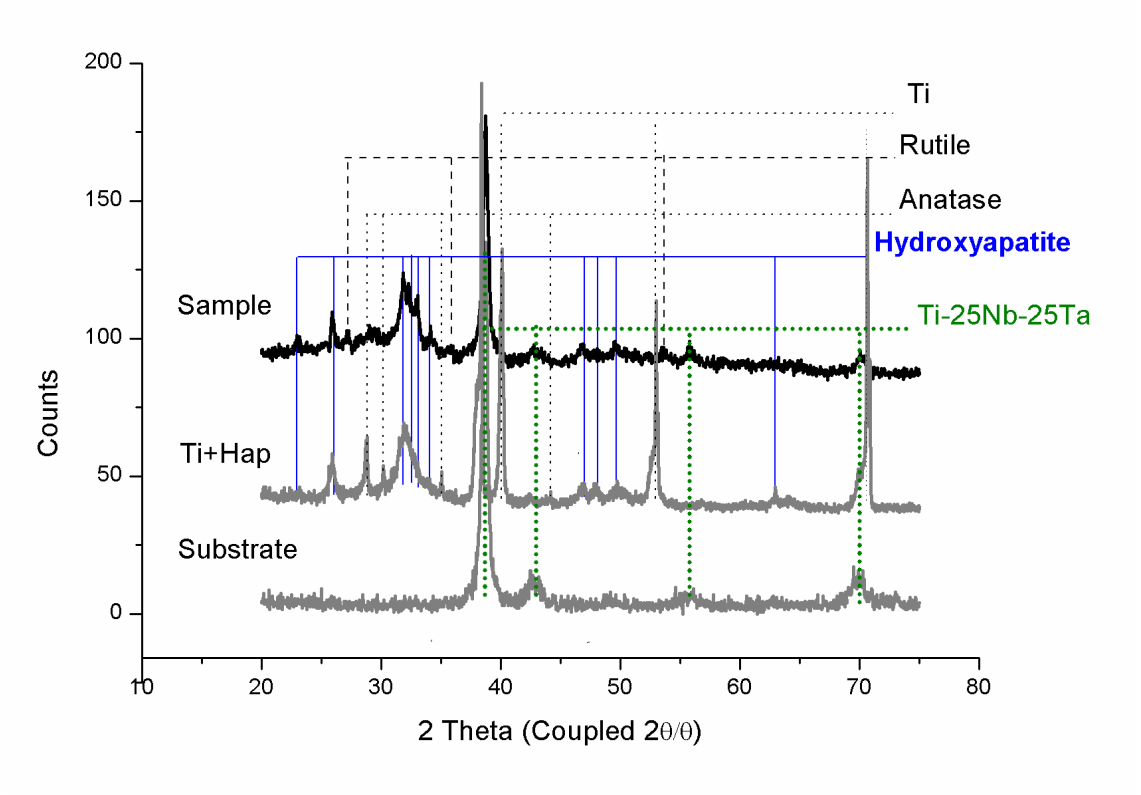
Ti
Rutile
Anatase
Hydroxyapatite
Ti-25Nb-25Ta
Sample
Ti+Hap
Substrate
Counts
2 Theta (Coupled 2θ/θ)
200
150
100
50
0
10
20
30
40
50
60
70
80

Figure 7.

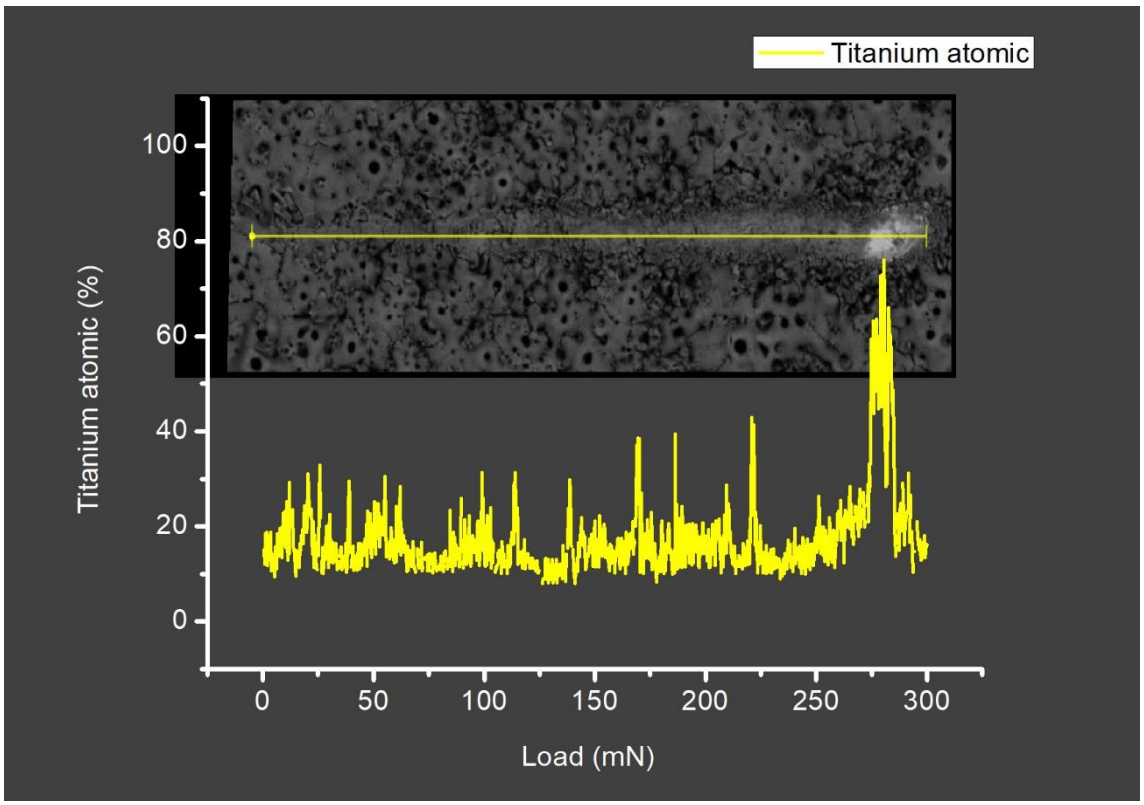
Titanium atomic
Titanium atomic (%)
100
80
60
40
20
0
0
50
100
150
200
250
300
Load (mN)

Figure 8.

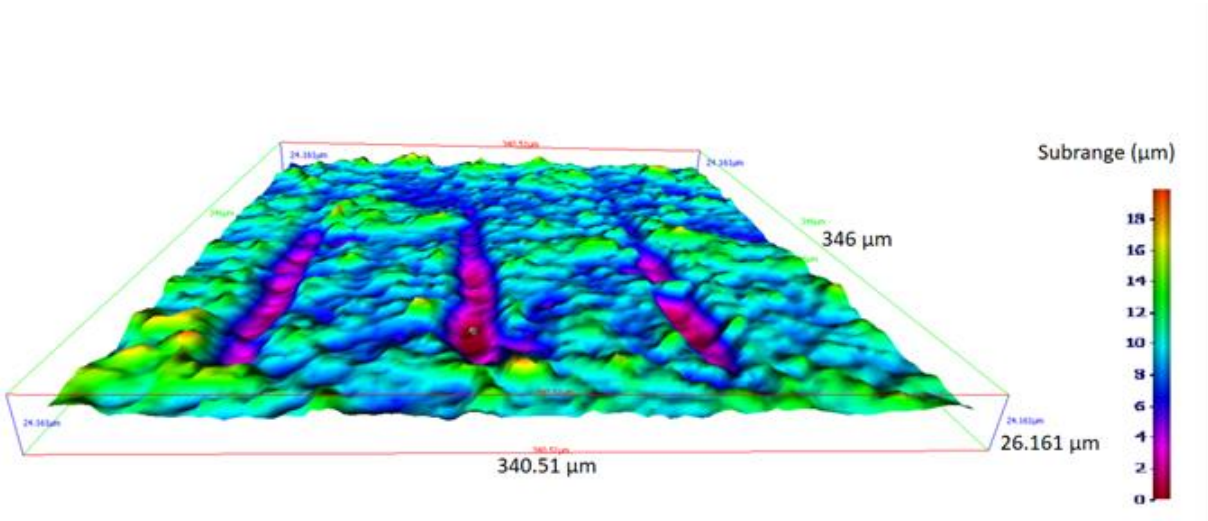

Figure 9.